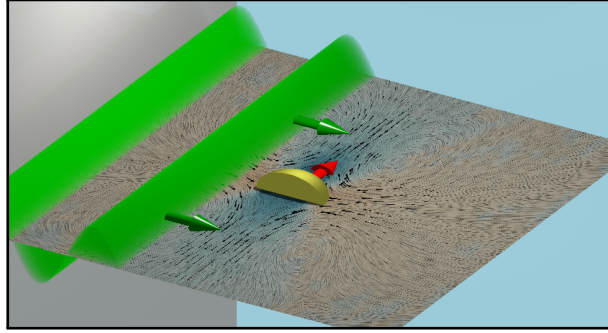


On the shape-dependent propulsion of nano- and microparticles by traveling ultrasound waves

Johannes Voß¹ and Raphael Wittkowski^{1,*}

¹*Institut für Theoretische Physik, Center for Soft Nanoscience,
Westfälische Wilhelms-Universität Münster, D-48149 Münster, Germany*

Among the many types of artificial motile nano- and microparticles that have been developed in the past, colloidal particles that exhibit propulsion when they are exposed to ultrasound are particularly advantageous. Their properties, however, are still largely unexplored. For example, the dependence of the propulsion on the particle shape and the structure of the flow field generated around the particles are still unknown. In this article, we address the propulsion mechanism of ultrasound-propelled nano- and microparticles in more detail. Based on direct computational fluid dynamics simulations and focusing on traveling ultrasound waves, we study the effect of two important aspects of the particle shape on the propulsion: rounded vs. pointed and filled vs. hollow shapes. We also address the flow field generated around such particles. Our results reveal that pointedness leads to an increase of the propulsion speed, whereas it is not significantly affected by hollowness. Furthermore, we find that the flow field of ultrasound-propelled particles allows to classify them as pusher squirmers, which has far-reaching consequences for the understanding of these particles and allows us to predict that they can be used to realize active materials with a tunable viscosity that can exhibit suprafluidity and even negative viscosities. The obtained results are helpful, e.g., for future experimental work further investigating or applying ultrasound-propelled colloidal particles as well as for theoretical approaches that aim at modeling their dynamics on mesoscopic scales.



I. INTRODUCTION

With the experimental discovery of fuel-less ultrasound-propelled (also called “self-acoustophoretic”) colloidal particles in 2012,¹ important potential applications of motile nano- and microparticles (also called “active particles”)² have become within reach.³ One of their most attractive potential applications is the usage as self-propelled nano- or microdevices in medicine^{4–6} that allows for targeted drug delivery,^{7–12} enhanced biodegradation,^{13,14} nanosurgery,^{15,16} enhanced diagnostics,^{4,17–19} and many more fascinating applications.^{16,20–27} In contrast to different propulsion mechanisms like chemical propulsion,^{20,28,29} other fuel-based propulsion,³⁰ light-propulsion,³¹ and X-Ray propulsion,³² the acoustic propulsion^{1,5–9,13,18,33–44} has important advantages: It is fuel-free, biocompatible, and allows to supply the particles continuously with energy. Ultrasound-propelled particles can be rigid^{1,7,9,33–38,41,42,44–47} or have moveable components.^{30,42,48,49} The latter ones include bubble-propelled particles,^{30,49} which can reach rather high

propulsion speeds, but since the former ones are easier to produce, they are more likely to be applied in the near future. There exist also hybrid particles combining acoustic propulsion with a different propulsion mechanism.^{37,40,44,50,51}

Ultrasound-propelled nano- and microparticles have been intensively investigated in recent years.^{1,33–35,38,39,41,42,44–47,52–54} While the most studies are based on experiments,^{1,33–35,38,39,41,42,44,47} there are only two theory-based studies so far.^{45,46} Despite the large number of existing studies on acoustically propelled particles, we are still at the beginning of exploring and understanding their features. Even the details of their propulsion mechanism are still unclear. For example, it is not yet known how the propulsion speed depends on the properties of the particles and their environment, what the maximal speed of the particles for a given ultrasound intensity is, and which structure the flow field generated around the particles has. One of the most basic properties of the particles is their shape. Nevertheless, only very few particle shapes have been considered so far. The main reason for this is that the

particle shape cannot easily be varied in experimental studies and that the existing theoretical studies focus on the particle shapes used in the experiments. The particle shapes studied so far are mostly cylinders with a concave and a convex end.^{1,34–36,47} As a limiting case, also cup-shaped particles were studied.^{38,44} Apart from that, there exist only a study that addresses gear-shaped particles⁴¹ and studies on particles with movable components^{30,42,48,49} and thus a nonconstant shape.

For a cylindrical shape with spherical concave and convex ends, the direction of movement was found in experiments to point towards the concave end,³⁹ but the two theoretical studies suggest that this depends on the shape of the caps.^{45,46} The direction of propulsion seems to depend also on the length of the cylinder, since cup-shaped particles were found to move towards their convex end.³⁸ Hence, we can conclude that the propulsion speed depends sensitively on the particles' shape, but we have not yet a deeper understanding of this dependence.

A better understanding of the shape-dependence of the propulsion would be helpful for future studies, since it would provide a good opportunity for optimizing the particle speed and thus the efficiency of the particles' propulsion. Large propulsion speeds are crucial for medical applications, where the maximal ultrasound intensity is limited by the requirement of biocompatibility and the particles must be fast enough to withstand the blood flow that tends to carry the particles away. The fastest ultrasound-propelled fuel-free particles observed so far reached a speed of about $250 \mu\text{m s}^{-1}$.³³ This is faster than the blood flow in the vascular capillaries with a typical speed of about $100 \mu\text{m s}^{-1}$,¹⁶ but the transducer voltage of 10 V applied in the corresponding experiments indicates that the acoustic energy density was about $10\text{--}100 \text{ J m}^{-3}$ ⁵⁵ and thus too high for usage in the human body, where the energy density should be below 4.9 J m^{-3} to avoid damage to the tissue.⁵⁶

A further limitation related to the experiments is the usage of a standing ultrasound wave in all but one⁴² experimental studies. To facilitate observation of the particles with a microscope, they are enclosed by a thin chamber with two parallel horizontal walls, of which at least the upper one is transparent, and a standing wave field that levitates the particles in a nodal plane between the horizontal walls of the chamber. However, in many important potential applications, such as medical ones, the sound waves would be traveling.

In this article, we advance the knowledge about the acoustic propulsion of homogeneous rigid nano- and microparticles that are exposed to traveling ultrasound waves. Using direct computational fluid dynamics simulations based on numerically solving the compressible Navier-Stokes equations, we determine the sound-induced forces acting on these particles together with their resulting propulsion speed as well as the flow field generated around the particles. To address the shape-dependence of these quantities, we consider some particle

shapes that differ with respect to two aspects not studied previously: We compare rounded with pointed shapes and filled with hollow ones.

II. METHODS

The setup for our study is shown in Fig. 1. A traveling

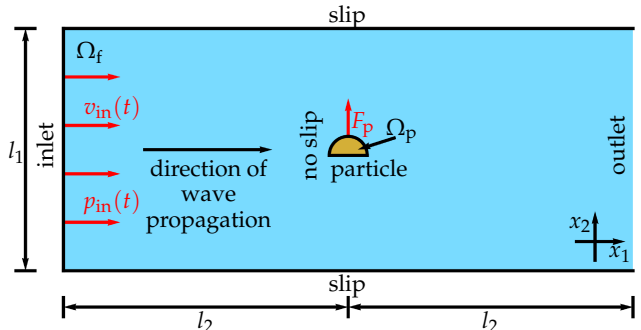


FIG. 1. Setup for the simulations. A traveling ultrasound wave is entering the fluid domain Ω_f at the inlet, where it is prescribed by an inflow velocity $v_{\text{in}}(t)$ and pressure $p_{\text{in}}(t)$. The width of the fluid domain is l_1 and the rigid particle, constituting a particle domain Ω_p , is placed at a distance l_2 from the inlet. At the particle boundary a no-slip condition is prescribed and for the lateral boundaries of Ω_f slip boundary conditions are used. The ultrasound exerts a time-averaged propulsion force F_p on the particle and after a further distance l_2 the domain Ω_f ends with an outlet.

ultrasound wave with frequency $f = 1 \text{ MHz}$ enters a rectangular domain Ω_f of an initially quiescent fluid, which we assume to be water, at an inlet of width $l_1 = 200\sigma$, where $\sigma = 1 \mu\text{m}$ is the particle diameter. At the inlet, the ultrasound wave is prescribed by a time-dependent inflow velocity $v_{\text{in}}(t) = (\Delta p / (\rho_0 c_f)) \sin(2\pi f t)$ perpendicular to the inlet and a time-dependent inflow pressure $p_{\text{in}}(t) = \Delta p \sin(2\pi f t)$ with the pressure amplitude $\Delta p = 10 \text{ kPa}$, the density of the quiescent fluid $\rho_0 = 998 \text{ kg m}^{-3}$, and the sound velocity in the fluid $c_f = 1484 \text{ m s}^{-1}$. The pressure amplitude corresponds to an acoustic energy density $E = \Delta p^2 / (2\rho_0 c_f^2) = 22.7 \text{ mJ m}^{-3}$. Starting at the inlet, the ultrasound wave propagates through the fluid domain parallel to its lateral boundaries, where we prescribe slip boundary conditions. After a distance $l_2 = \lambda/4$ with the wavelength of the ultrasound $\lambda = 1.484 \text{ mm}$, the wave arrives the fixed rigid particle, which is oriented perpendicular to the propagation direction of the wave. In the simulations, we describe the particle by a particle domain Ω_p and prescribe no-slip conditions at the particle's boundary $\partial\Omega_p$. Through the ultrasound, a propulsion force F_p parallel to the particle's orientation is exerted on the particle. The wave then propagates a further distance l_2 until it reaches an outlet at the end of the domain Ω_f .

To avoid approximations like perturbation expansions that are involved in all previous studies using analytical^{45,46} or numerical^{41,42,44} methods to determine

the propulsion speed of acoustically propelled particles, we base our work on direct fluid dynamics simulations. Our simulations are carried out by numerically solving the compressible Navier-Stokes equations together with the continuity equation for the mass-density field $\rho(\vec{x}, t)$ of the fluid and a constitutive equation for the fluid's pressure field $p(\vec{x}, t)$ in the two-dimensional fluid domain Ω_f . Here, $\vec{x} = (x_1, x_2)^T$ is the position vector and t denotes time.

When $\vec{v}(\vec{x}, t)$ with $\vec{v} = (v_1, v_2)^T$ is the velocity field of the fluid and we use the short notation $\partial_i = \partial/\partial x_i$ with $i \in \{1, 2\}$ for the spatial derivatives, the *continuity equation* that describes mass conservation is given by⁵⁷

$$\frac{\partial \rho}{\partial t} + \sum_{i=1}^2 \partial_i(\rho v_i) = 0. \quad (1)$$

Momentum conservation of the fluid is then described by the *Navier-Stokes equations*⁵⁷

$$\frac{\partial}{\partial t}(\rho v_i) + \sum_{j=1}^2 \partial_j \Pi_{ij} = 0 \quad (2)$$

with the momentum-current tensor

$$\Pi_{ij} = \rho v_i v_j - \Sigma_{ij} \quad (3)$$

and the stress tensor

$$\Sigma_{ij} = \Sigma_{ij}^{(p)} + \Sigma_{ij}^{(v)} \quad (4)$$

for $i, j \in \{1, 2\}$. The stress tensor consists of the pressure part

$$\Sigma_{ij}^{(p)} = -p \delta_{ij} \quad (5)$$

and viscous part

$$\begin{aligned} \Sigma_{ij}^{(v)} = & \nu_s \left(\partial_j v_i + \partial_i v_j - \frac{2}{3} \sum_{k=1}^2 (\partial_k v_k) \delta_{ij} \right) \\ & + \nu_b \sum_{k=1}^2 (\partial_k v_k) \delta_{ij} \end{aligned} \quad (6)$$

with the Kronecker symbol δ_{ij} , shear viscosity (also called “dynamic viscosity”) ν_s , and bulk viscosity (also called “volume viscosity”) ν_b . Heat conduction and heating of the fluid by the sound waves are neglected here, since the ultrasound intensities that are used in experiments with acoustically-propelled colloidal particles are usually rather small. To close the set of Eqs. (1)-(6), we need a constitutive equation for the pressure $p(\vec{x}, t)$. When the sound intensity is sufficiently small, so that the fluid is acoustically nondispersive and heating of the fluid by the sound wave can be neglected, the local pressure $p(\vec{x}, t)$ is given by the *constitutive equation*

$$p(\rho) = p_0 + c_f^2(\rho - \rho_0) \quad (7)$$

as a function of the local mass density $\rho(\vec{x}, t)$. Here, c_f is the speed of sound in the fluid and ρ_0 and $p_0 = p(\rho_0)$ are the constant mean mass density and pressure of the fluid, respectively. To solve Eqs. (1)-(7) numerically, we used the software package OpenFOAM,⁵⁸ which applies the finite volume method.

The time-dependent force $\vec{F}_p(t)$ with $\vec{F}_p = (F_{p,1}, F_{p,2})^T$ acting on the particle is calculated in the laboratory frame. Since the particle, which is described by the particle domain Ω_p , has no-slip boundary conditions and is fixed in space in our simulations, the fluid velocity $\vec{v}(\vec{x}, t)$ is zero at the fluid-particle interface $\partial\Omega_p$. So the force acting on the particle is given by $\vec{F}_p = \vec{F}^{(p)} + \vec{F}^{(v)}$ with the components⁵⁷

$$F_i^{(\alpha)} = \sum_{j=1}^2 \int_{\partial\Omega_p} \Sigma_{ij}^{(\alpha)} dA_j, \quad \alpha \in \{p, v\}. \quad (8)$$

Here, $d\vec{A}(\vec{x})$ with $d\vec{A} = (dA_1, dA_2)^T$ is the normal and outwards oriented surface element of $\partial\Omega_p$ at position \vec{x} when $\vec{x} \in \partial\Omega_p$. By time-averaging $\vec{F}^{(p)}(t)$ and $\vec{F}^{(v)}(t)$ locally over one period τ of the ultrasound wave in the stationary state (i.e., for large t), we obtain the time-averaged stationary forces $\langle \vec{F}^{(p)} \rangle$, $\langle \vec{F}^{(v)} \rangle$, and $\langle \vec{F}_p \rangle = \langle \vec{F}^{(p)} \rangle + \langle \vec{F}^{(v)} \rangle$, where $\langle \cdot \rangle$ denotes the time average. Using $\langle \vec{F}_p \rangle$, we then calculate the time-averaged stationary propulsion velocity^{59,60}

$$\langle \vec{v}_p \rangle = \frac{1}{\nu_s} \mathbf{K}^{-1} \langle \vec{F}_p \rangle \quad (9)$$

with the resistance matrix \mathbf{K} of the considered particle, which is determined using the software **HydResMat**.^{60,61} As we simulate a two-dimensional system to keep the computational effort manageable, but \mathbf{K} is a 3×3 -dimensional matrix that corresponds to a three-dimensional particle, we cannot apply Eqs. (8) and (9) directly. Therefore, we assign a thickness of σ to the particle, which equals its diameter, so that \mathbf{K} can be calculated. Neglecting contributions by the lower and upper surfaces of the particle, we then use the three-dimensional versions of Eqs. (8) and (9). From $\langle \vec{F}_p \rangle$ and $\langle \vec{v}_p \rangle$, we directly obtain the propulsion force $F_p = (\langle \vec{F}_p \rangle)_2 = F_{p,p} + F_{p,v}$, its pressure component $F_{p,p} = (\langle \vec{F}^{(p)} \rangle)_2$ and viscous component $F_{p,v} = (\langle \vec{F}^{(v)} \rangle)_2$, as well as the propulsion speed $v_p = (\langle \vec{v}_p \rangle)_2$ as the force- and velocity contributions parallel to the particle's orientation, i.e., parallel to the x_2 axis.

Nondimensionalization of the equations introduced above leads to the Helmholtz number He , a Reynolds number corresponding to the shear viscosity Re_s , another Reynolds number corresponding to the bulk viscosity Re_b , and the product $Ma^2 Eu$, with the Mach number Ma and Euler number Eu , corresponding to the pressure amplitude Δp of the ultrasound wave that enters the simulated system. Table I shows the names, symbols, and assigned values of the parameters that are relevant for our simulations. The parameters related to the

Name	Symbol	Value
Particle diameter	σ	1 μm
Sound frequency	f	1 MHz
Speed of sound	c_f	1484 m s^{-1}
Time period of sound	$\tau = 1/f$	1 μs
Wavelength of sound	$\lambda = c_f/f$	1.484 mm
Mean mass density of fluid	ρ_0	998 kg m^{-3}
Mean pressure of fluid	p_0	101 325 Pa
Initial velocity of fluid	\vec{v}_0	$\vec{0} \text{ m s}^{-1}$
Sound pressure amplitude	Δp	10 kPa
Acoustic energy density	$E = \Delta p^2 / (2\rho_0 c_f^2)$	22.7 mJ m^{-3}
Shear/dynamic viscosity of fluid	ν_s	1.002 mPa s
Bulk/volume viscosity of fluid	ν_b	2.87 mPa s
Domain width	l_1	200 σ
Inlet-particle or particle-outlet distance	l_2	$\lambda/4$
Mesh-cell size	Δx	15 nm-1 μm
Time-step size	Δt	1-10 ps
Simulation duration	t_{max}	500 τ

TABLE I. Parameters that are relevant for our simulations and their values. We obtained the bulk viscosity ν_b for water at temperature $T = 293.15 \text{ K}$ by a cubic spline interpolation of the data from Tab. 1 in Ref. 62.

fluid are based on assuming that the fluid is water at normal temperature $T = 293.15 \text{ K}$ and normal pressure $p_0 = 101\,325 \text{ Pa}$. With the parameter values from Tab. I, our simulations correspond to the following values of the dimensionless numbers:

$$\text{He} = 2\pi f \sigma / c_f \approx 4.234 \cdot 10^{-3}, \quad (10)$$

$$\text{Re}_s = \rho_0 c_f \sigma / \nu_s \approx 1478, \quad (11)$$

$$\text{Re}_b = \rho_0 c_f \sigma / \nu_b \approx 516, \quad (12)$$

$$\text{Ma}^2 \text{Eu} = \Delta p / (\rho_0 c_f^2) \approx 4.550 \cdot 10^{-6}. \quad (13)$$

We discretized the fluid domain Ω_f using a structured mixed rectangular-triangular mesh with about 250,000 cells. The typical cell size Δx varied from about 15 nm near the particle to about 1 μm far away from the particle. For the time integration, we used an adaptive time-step method with a maximum time-step size ensuring that the Courant-Friedrichs-Lewy number

$$C = c_f \frac{\Delta t}{\Delta x} \quad (14)$$

is smaller than one. The typical time-step size Δt was thus between 1 ps and 10 ps. The simulations ran for $t_{\text{max}} = 500\tau$ to get sufficiently close to the stationary state. Due to the fine discretization in space and time and the relatively large spatial and temporal domains, the simulations were computationally very expensive and required a strong parallelization. The typical duration of one simulation was about 36,000 CPU core hours.

Since the simulations would require even more time to fully converge, we determined the stationary forces $F_{p,p}$ and $F_{p,v}$ by extrapolation. For this purpose, we used the

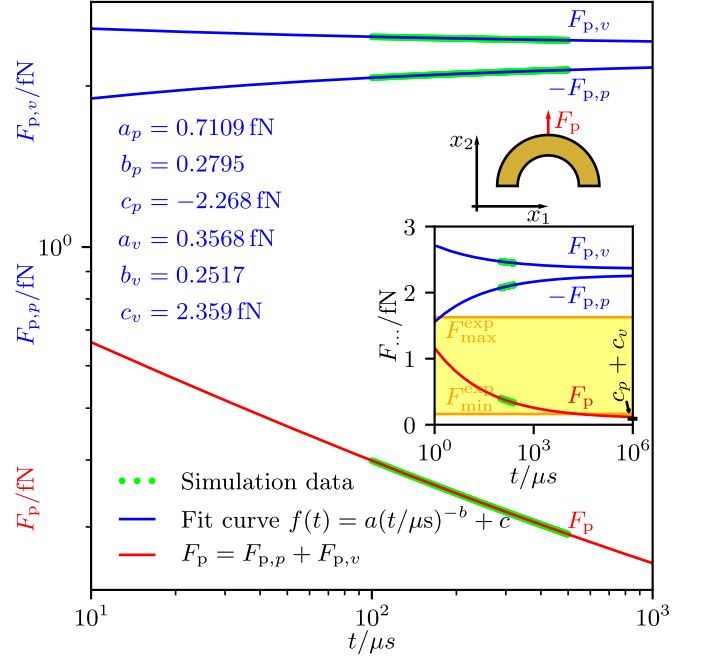


FIG. 2. Simulation data for the time-dependent forces $F_{p,p}(t)$ and $F_{p,v}(t)$ acting on a particle with the shape of a hollow half ball as well as an extrapolation of the forces with the fit function $f(t)$. The extrapolation of the total propulsion force $F_p(t) = F_{p,p}(t) + F_{p,v}(t)$ converges against $c_p + c_v$, where c_p and c_v are the offset fit coefficients in $f(t)$ for $F_{p,p}(t)$ and $F_{p,v}(t)$, respectively. Its limiting value is consistent with corresponding experimental data from Soto *et al.*³⁸ that can be tied to the interval $[F_{\text{min}}^{\text{exp}}, F_{\text{max}}^{\text{exp}}] = [0.163 \text{ fN}, 1.63 \text{ fN}]$.

fit function

$$f(t) = a \left(\frac{t}{\mu\text{s}} \right)^{-b} + c. \quad (15)$$

An example for the extrapolation, corresponding to a hollow-half-ball particle, is shown in Fig. 2. In the inset of this figure, the experimental data³⁸ available for this particle shape are indicated by a yellow band. The values of the fit parameters for all considered particle shapes are listed in Tab. II.

III. RESULTS AND DISCUSSION

Since we are interested in studying the effect of point-ness and hollowness on the particle propulsion, we consider four different particle shapes: a half ball, a cone, and hollowed-out versions of both shapes (see Fig. 3). All considered particles have diameter σ and the hollow ones have wall width $\sigma/5$. Both the particles' center of mass (CoM) and center of resistance (CoR) are on the symmetry axes of the particles. These particle shapes are chosen, since they are relatively simple with an axis of rotational symmetry, have a head-tail asymmetry that is necessary for acoustic propulsion, and differ with re-

Fit parameter	Half ball	Cone	Hollow half ball	Hollow cone
a_p	0.5188 fN	0.7301 fN	0.7109 fN	0.9332 fN
b_p	0.2825	0.2919	0.2795	0.2808
c_p	-2.995 fN	-6.455 fN	-2.268 fN	-6.007 fN
a_v	0.2506 fN	0.2033 fN	0.3568 fN	0.2686 fN
b_v	0.2447	0.2180	0.2517	0.2104
c_v	3.073 fN	6.943 fN	2.359 fN	6.529 fN

TABLE II. Fit parameters of the function (15) for the force components $F_{p,p}$ (index p) and $F_{p,v}$ (index v) for each considered particle shape. The second-last column corresponds to Fig. 2.

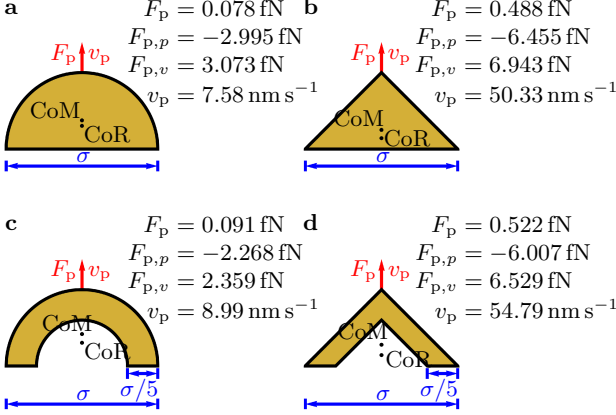


FIG. 3. The considered particle shapes: (a) half ball, (b) cone, (c) hollow half ball, and (d) hollow cone. All particles have diameter σ and the hollow particles have wall width $\sigma/5$. The center of mass (CoM), the center of resistance (CoR), and the direction of the propulsion force F_p and corresponding propulsion speed v_p , which are parallel to the symmetry axes of the particles and perpendicular to the main direction of sound propagation, are indicated. For each particle shape, the values of $F_p = F_{p,p} + F_{p,v}$, the pressure component $F_{p,p}$, the viscous component $F_{p,v}$, and v_p are given.

spect to pointedness and hollowness. The half ball is neither pointed nor hollow, the cone is pointed but not hollow, the hollow half ball is not pointed but hollow, and the hollow cone is both pointed and hollow. Due to the huge computational expense of the simulations, we did not consider additional particle shapes. A further motivation for choosing the mentioned particle shapes is the fact that there exist experimental data from a previous study that considered cup-shaped particles that are similar to our hollow half ball.³⁸

Figure 3 shows also the results for the propulsion force $F_p = F_{p,p} + F_{p,v}$, its pressure component $F_{p,p}$ and viscous component $F_{p,v}$, and the corresponding propulsion speed v_p . For all particle shapes, F_p and v_p are positive. The components $F_{p,p}$ and $F_{p,v}$ are always negative and positive, respectively, where the latter component is dominating. Remarkably, both cone-shaped particles are associated with propulsion speeds $v_p \approx 50 \text{ nm s}^{-1}$ that are one order of magnitude larger than those for the half-ball shapes. This suggests that pointed shapes allow much faster acoustic propulsion than rounded ones. Compar-

ing the corresponding filled and hollowed-out particle shapes reveals that the hollow particles reach slightly (less than 20 percent) larger propulsion speeds than their filled counterparts. This suggests that cavities in the particles have no significant effect on their propulsion speed. Among the considered particles, that with a hollow-cone shape reaches the largest propulsion force $F_p = 0.522 \text{ fN}$ and the largest propulsion speed $v_p = 54.79 \text{ nm s}^{-1}$.

Our result for v_p for the hollow-half-ball particle can be compared to results from experiments described in Ref. 38, where particles with a similar shape and size were found to propel with speed $v_p = 82.4(54) \mu\text{m s}^{-1}$. However, the comparison is complicated by the fact that this reference mentions not the acoustic energy density the particles were exposed to, but instead, as it is usual in experimental studies on acoustically propelled particles, only the amplitude of the alternating voltage applied to the piezoelectric transducer. To estimate the energy density that is related to the known voltage amplitude, we use the typical energy-density values for some voltage ranges given in Ref. 55. According to this reference, a voltage amplitude lower than 10 V, as is used in the experiments described in Ref. 38, is typically associated with an acoustic energy density of $10\text{-}100 \text{ J m}^{-3}$. In our simulations, the energy density was 22.7 mJ m^{-3} and thus much smaller than in the experiments. Calculating the propulsion force F_p that corresponds to the propulsion speed v_p reported in the experiments and assuming that this force scales linearly with the acoustic energy density, we find a range of force values $[F_{\min}^{\text{exp}}, F_{\max}^{\text{exp}}]$ with $F_{\min}^{\text{exp}} = 0.163 \text{ fN}$ and $F_{\max}^{\text{exp}} = 1.63 \text{ fN}$ that could have been observed in the experiments when using the same energy density as in our simulations. This is consistent with our finding for F_p . To be precise, our value for F_p is slightly below F_{\min}^{exp} , but given that F_{\min}^{exp} and F_{\max}^{exp} have been determined by a rough estimate, that we simulated traveling ultrasound waves whereas the experiments involved standing waves, and that the frequency of the ultrasound was different in the simulations and experiments, the agreement of the force interval estimated from the experimental data with our result is very good.

Next, we study the flow field around the particles. Figure 4 shows the time-averaged mass-current density $\langle \rho \vec{v} \rangle$ and reduced pressure $\langle p - p_0 \rangle$ for all considered particles. In each case, the far field of the flow shows two large counter-rotating vortices with diameters of about 100σ ,

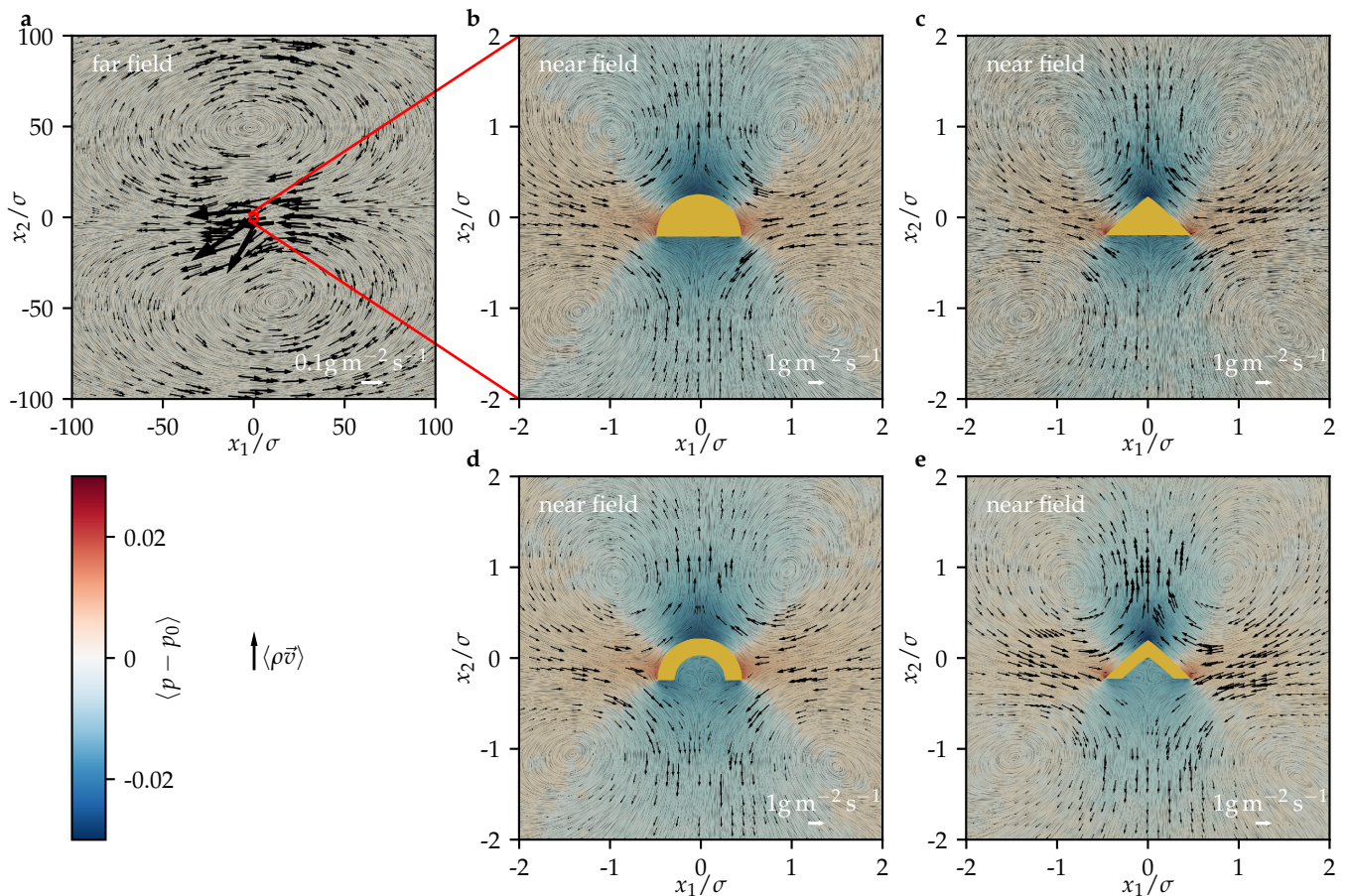


FIG. 4. The time-averaged mass-current density $\langle \rho \vec{v} \rangle$ and reduced pressure $\langle p - p_0 \rangle$ for all considered particle shapes (see Fig. 3). (a) The far field is shown for a half-ball particle and looks similar for the other particle shapes; (b)-(e) The near field is shown for each particle shape.

which are in front of and behind the particle, respectively. Such a flow field is typical for acoustic streaming around a particle exposed to ultrasound even for simple shapes like a sphere.⁶³ Also the near field of the flow is similar for all considered particle shapes. The structure of the near field, however, is qualitatively different from that of the far field. There are now four vortices to the left and right in front of and behind the particles. The diameter of these vortices is about 2σ . There is an inflow towards the particles from their left and right and an outflow away from the particles at their front and back. For the reduced pressure, negative values are observed in front of and behind the particles, whereas positive values are observed to their left and right.

Such flow fields are well-known from squirmers.^{64,65} Comparing the flow near fields observed in our simulations with those from different types of squirmers, our particles can be identified as *pushers*. The identification of the acoustically-propelled particles as pushers is an important discovery, since it allows to translate the known properties of and modeling techniques for pushers to the so far much less investigated acoustically-propelled particles. Our results for the flow fields suggest that they are

caused by local acoustic streaming close to the particles, as predicted in the theoretical work 45.

IV. CONCLUSIONS

Based on direct numerical simulations, we have studied the acoustic propulsion of nonspherical nano- and microparticles by traveling ultrasound. For particle shapes that were either rounded or pointed and either filled or hollow, we have calculated the propulsion force acting on the particle, the resulting propulsion speed, as well as the flow field around the particle. This allowed us to obtain important new insights into the propulsion of such particles. Our results, which are consistent with experiments from Soto *et al.*³⁸ for cup-shaped particles, confirmed that the particles' propulsion is very sensitive to the particle shape.⁴⁶ The results revealed that a particle with a pointed shape can show a much more efficient propulsion than one with a rounded shape and that a cavity in the particle shape has no significant effect on the propulsion efficiency. Considering the small number of different particle shapes that have been addressed

in previous studies, these findings suggest to use conical particles in future studies further investigating or applying acoustically-propelled colloidal particles to reach higher propulsion speeds than for cup-shaped particles³⁸ and the commonly used bullet-shaped particles.^{1,33,34,39} Since we found only a negligible effect of a cavity in the particle shape on its propulsion efficiency, the conical particle can have or have not a cavity, depending on which particle shape is easier to synthesize. Knowing that the propulsion efficiency of the particles can significantly be enhanced by choosing a more suitable particle shape is an important insight with respect to potential applications of this type of active particles, e.g., in nanomedicine, where the particles need a large propulsion speed to withstand blood flow while the ultrasound intensity is limited to physiologically harmless values.^{16,66,67} When the particles shall be used for drug delivery in nanomedicine, a filled particle is advantageous, as its larger volume is associated with a larger capacity for transporting drugs.

The obtained time-averaged flow fields support the understanding of the particles' propulsion mechanism as originating basically from local acoustic streaming, as predicted by Nadal and Lauga.⁴⁵ Remarkably, the flow's near field allowed us to identify the particles as pusher squirmers, which strongly extends our understanding of ultrasound-propelled nano- and microparticles. This finding allows to transfer the large existing knowledge about the motion of pushers and, e.g., their interactions with obstacles and other particles to ultrasound-propelled particles, for which most of these issues have not yet been addressed. We expect that this will strongly boost the future theoretical investigation of ultrasound-propelled colloidal particles. For example, one could now use modified squirmer models to describe the motion of the particles on much larger time scales, which are no longer set by the high frequency of the ultrasound but

instead by the rather small time-averaged flow velocities near the particles. This would reduce the computational effort to simulate the motion of the particles by several orders of magnitude and enable studies that were well-nigh impossible up to now. In addition, such modeling would even allow for the application of new analytical approaches, such as field theories for describing the collective dynamics of many interacting particles on mesoscopic or macroscopic scales.^{68–72} Furthermore, the identification of the ultrasound-propelled particles as pushers has intriguing consequences for future materials science. Since it is known from suspensions of bacteria that pushers can strongly reduce the viscosity of a liquid, we can predict that it is possible to use suspensions of ultrasound-propelled particles to realize novel active materials with a viscosity that can be tuned via the ultrasound intensity from the normal positive viscosity of the suspension in the absence of ultrasound through to suprafluidity up to even negative viscosities.^{73,74}

Apart from that, the basic understanding of the details of the particles' propulsion mechanism should further be extended by additional computational fluid dynamics simulations. As a task for the future, e.g., the dependence of the propulsion efficiency on the aspect ratio of conical particles should be studied in detail. Examples for other parameters, whose influence on the particles' propulsion still needs to be studied, are the viscosity of the fluid and the frequency of the ultrasound.

ACKNOWLEDGMENTS

We thank Patrick Kurzeja for helpful discussions. R.W. is funded by the Deutsche Forschungsgemeinschaft (DFG, German Research Foundation) – WI 4170/3-1. The simulations for this work were performed on the computer cluster PALMA II of the University of Münster.

* Corresponding author: raphael.wittkowski@uni-muenster.de

¹ W. Wang, L. Castro, M. Hoyos, and T. E. Mallouk, "Autonomous motion of metallic microrods propelled by ultrasound," *ACS Nano* **6**, 6122–6132 (2012).

² C. Bechinger, R. Di Leonardo, H. Löwen, C. Reichhardt, G. Volpe, and G. Volpe, "Active particles in complex and crowded environments," *Reviews of Modern Physics* **88**, 045006 (2016).

³ T. Xu, L. Xu, and X. Zhang, "Ultrasound propulsion of micro-/nanomotors," *Applied Materials Today* **9**, 493–503 (2017).

⁴ K. Kim, J. Guo, Z. Liang, and D. Fan, "Artificial micro/nanomachines for bioapplications: biochemical delivery and diagnostic sensing," *Advanced Functional Materials* **28**, 1705867 (2018).

⁵ Z. Wu *et al.*, "Turning erythrocytes into functional micromotors," *ACS Nano* **8**, 12041–12048 (2014).

⁶ Z. Wu, B. Esteban-Fernández de Ávila, A. Martín,

C. Christianson, W. Gao, S. K. Thamphiwatana, A. Escarpa, Q. He, L. Zhang, and J. Wang, "RBC micromotors carrying multiple cargos towards potential theranostic applications," *Nanoscale* **7**, 13680–13686 (2015).

⁷ V. Garcia-Gradilla, S. Sattayasamitsathit, F. Soto, F. Kuralay, C. Yardımcı, D. Wiitala, M. Galarnyk, and J. Wang, "Ultrasound-propelled nanoporous gold wire for efficient drug loading and release," *Small* **10**, 4154–4159 (2014).

⁸ B. Esteban-Fernández de Ávila, D. E. Ramírez-Herrera, S. Campuzano, P. Angsantikul, L. Zhang, and J. Wang, "Nanomotor-enabled pH-responsive intracellular delivery of caspase-3: toward rapid cell apoptosis," *ACS Nano* **11**, 5367–5374 (2017).

⁹ M. Uygun, B. Jurado-Sánchez, D. A. Uygun, V. V. Singh, L. Zhang, and J. Wang, "Ultrasound-propelled nanowire motors enhance asparaginase enzymatic activity against cancer," *Nanoscale* **9**, 18423–18429 (2017).

¹⁰ M. Luo, Y. Feng, T. Wang, and J. Guan, "Micro-/nanorobots at work in active drug delivery," *Advanced*

- Functional Materials **28**, 1706100 (2018).
- 11 W. Wang, S. Li, L. Mair, S. Ahmed, T. J. Huang, and T. E. Mallouk, "Acoustic propulsion of nanorod motors inside living cells," *Angewandte Chemie International Edition* **53**, 3201–3204 (2014).
 - 12 B. Esteban-Fernández de Ávila, C. Angell, F. Soto, M. A. Lopez-Ramirez, D. F. Báez, S. Xie, J. Wang, and Y. Chen, "Acoustically propelled nanomotors for intracellular siRNA delivery," *ACS Nano* **10**, 4997–5005 (2016).
 - 13 Z. Wu, T. Li, W. Gao, W. Xu, B. Jurado-Sánchez, J. Li, W. Gao, Q. He, L. Zhang, and J. Wang, "Cell-membrane-coated synthetic nanomotors for effective biodegradation," *Advanced Functional Materials* **25**, 3881–3887 (2015).
 - 14 B. Esteban-Fernández de Ávila, P. Angsantikul, D. E. Ramírez-Herrera, F. Soto, H. Teymourian, D. Dehaini, Y. Chen, L. Zhang, and J. Wang, "Hybrid biomembrane-functionalized nanorobots for concurrent removal of pathogenic bacteria and toxins," *Science Robotics* **3**, eaat0485 (2018).
 - 15 J. Li, B. Esteban-Fernández de Ávila, W. Gao, L. Zhang, and J. Wang, "Micro/nanorobots for biomedicine: delivery, surgery, sensing, and detoxification," *Science Robotics* **2**, eaam6431 (2017).
 - 16 P. Erkoç, I. C. Yasa, H. Ceylan, O. Yasa, Y. Alapan, and M. Sitti, "Mobile microrobots for active therapeutic delivery," *Advanced Therapeutics* **2**, 1800064 (2019).
 - 17 A. Chalupniak, E. Morales-Narváez, and A. Merkoci, "Micro and nanomotors in diagnostics," *Advanced Drug Delivery Reviews* **3**, 104–116 (2015).
 - 18 J. R. Qualliotine, G. Bolat, M. Beltrán-Gastélum, B. Esteban-Fernández de Ávila, J. Wang, and J. A. Califano, "Acoustic nanomotors for detection of human papillomavirus-associated head and neck cancer," *Otolaryngology–Head and Neck Surgery* **161**, 814–822 (2019).
 - 19 B. Esteban-Fernández de Ávila, A. Martín, F. Soto, M. A. Lopez-Ramirez, S. Campuzano, G. M. Vásquez-Machado, W. Gao, L. Zhang, and J. Wang, "Single cell real-time miRNAs sensing based on nanomotors," *ACS Nano* **9**, 6756–6764 (2015).
 - 20 F. Peng, Y. Tu, and D. A. Wilson, "Micro/nanomotors towards in vivo application: cell, tissue and biofluid," *Chemical Society Reviews* **46**, 5289–5310 (2017).
 - 21 F. Soto and R. Chrostowski, "Frontiers of medical micro/manorobotics: in vivo applications and commercialization perspectives toward clinical uses," *Frontiers in Bioengineering and Biotechnology* **6**, 170 (2018).
 - 22 W. He, J. Frueh, N. Hu, L. Liu, M. Gai, and Q. He, "Guidable thermophoretic Janus micromotors containing gold nanocolorifiers for infrared laser assisted tissue welding," *Advanced Science* **3**, 1600206 (2016).
 - 23 S. Balasubramanian *et al.*, "Micromachine-enabled capture and isolation of cancer cells in complex media," *Angewandte Chemie International Edition* **50**, 4161–4164 (2011).
 - 24 W. Gao, B. Esteban-Fernández de Ávila, L. Zhang, and J. Wang, "Targeting and isolation of cancer cells using micro/nanomotors," *Advanced Drug Delivery Reviews* **125**, 94–101 (2018).
 - 25 J. Hu, S. Huang, L. Zhu, W. Huang, Y. Zhao, K. Jin, and Q. ZhuGe, "Tissue plasminogen activator-porous magnetic microrods for targeted thrombolytic therapy after ischemic stroke," *ACS Applied Materials & Interfaces* **10**, 32988–32997 (2018).
 - 26 T. Xu, W. Gao, L.-P. Xu, X. Zhang, and S. Wang, "Fuel-free synthetic micro-/nanomachines," *Advanced Materials* **29**, 1603250 (2017).
 - 27 D. Wang, C. Gao, W. Wang, M. Sun, B. Guo, H. Xie, and Q. He, "Shape-transformable, fusible rodlike swimming liquid metal nanomachine," *ACS Nano* **12**, 10212–10220 (2018).
 - 28 B. Esteban-Fernández de Ávila, P. Angsantikul, J. Li, W. Gao, L. Zhang, and J. Wang, "Micromotors go in vivo: from test tubes to live animals," *Advanced Functional Materials* **28**, 1705640 (2018).
 - 29 M. Safdar, S. U. Khan, and J. Jänis, "Progress toward catalytic micro- and nanomotors for biomedical and environmental applications," *Advanced Materials* **30**, 1703660 (2018).
 - 30 D. Kagan, M. J. Benchimol, J. C. Claussen, E. Chuluun-Erdene, S. Esener, and J. Wang, "Acoustic droplet vaporization and propulsion of perfluorocarbon-loaded microbubbles for targeted tissue penetration and deformation," *Angewandte Chemie International Edition* **51**, 7519–7522 (2012).
 - 31 M. Xuan, J. Shao, C. Gao, W. Wang, L. Dai, and Q. He, "Self-propelled nanomotors for thermomechanically percolating cell membranes," *Angewandte Chemie International Edition* **57**, 12463–12467 (2018).
 - 32 Z. Xu, M. Chen, H. Lee, S.-P. Feng, J. Y. Park, S. Lee, and J. T. Kim, "X-ray-powered micromotors," *ACS Applied Materials & Interfaces* **11**, 15727–15732 (2019).
 - 33 V. Garcia-Gradilla, J. Orozco, S. Sattayasamitsathit, F. Soto, F. Kuralay, A. Pourazary, A. Katzenberg, W. Gao, Y. Shen, and J. Wang, "Functionalized ultrasound-propelled magnetically guided nanomotors: toward practical biomedical applications," *ACS Nano* **7**, 9232–9240 (2013).
 - 34 S. Ahmed, W. Wang, L. O. Mair, R. D. Fraleigh, S. Li, L. A. Castro, M. Hoyos, T. J. Huang, and T. E. Mallouk, "Steering acoustically propelled nanowire motors toward cells in a biologically compatible environment using magnetic fields," *Langmuir* **29**, 16113–16118 (2013).
 - 35 A. L. Balk, L. O. Mair, P. P. Mathai, P. N. Patrone, W. Wang, S. Ahmed, T. E. Mallouk, J. A. Liddle, and S. M. Stavis, "Kilohertz rotation of nanorods propelled by ultrasound, traced by microvortex advection of nanoparticles," *ACS Nano* **8**, 8300–8309 (2014).
 - 36 S. Ahmed, D. T. Gentekos, C. A. Fink, and T. E. Mallouk, "Self-assembly of nanorod motors into geometrically regular multimers and their propulsion by ultrasound," *ACS Nano* **8**, 11053–11060 (2014).
 - 37 W. Wang, W. Duan, Z. Zhang, M. Sun, A. Sen, and T. E. Mallouk, "A tale of two forces: simultaneous chemical and acoustic propulsion of bimetallic micromotors," *Chemical Communications* **51**, 1020–1023 (2015).
 - 38 F. Soto, G. L. Wagner, V. Garcia-Gradilla, K. T. Gillespie, D. R. Lakshmipathy, E. Karshalev, C. Angell, Y. Chen, and J. Wang, "Acoustically propelled nanoshells," *Nanoscale* **8**, 17788–17793 (2016).
 - 39 S. Ahmed, W. Wang, L. Bai, D. T. Gentekos, M. Hoyos, and T. E. Mallouk, "Density and shape effects in the acoustic propulsion of bimetallic nanorod motors," *ACS Nano* **10**, 4763–4769 (2016).
 - 40 L. Ren, D. Zhou, Z. Mao, P. Xu, T. J. Huang, and T. E.

- Mallouk, "Rheotaxis of bimetallic micromotors driven by chemical-acoustic hybrid power," *ACS Nano* **11**, 10591–10598 (2017).
- ⁴¹ S. Sabrina, M. Tasinkevych, S. Ahmed, A. M. Brooks, M. Olvera de la Cruz, T. E. Mallouk, and K. J. M. Bishop, "Shape-directed microspinners powered by ultrasound," *ACS Nano* **12**, 2939–2947 (2018).
 - ⁴² D. Ahmed, T. Baasch, B. Jang, S. Pane, J. Dual, and B. J. Nelson, "Artificial swimmers propelled by acoustically activated flagella," *Nano Letters* **16**, 4968–4974 (2016).
 - ⁴³ X. Lu, H. Shen, Z. Wang, K. Zhao, H. Peng, and W. Liu, "Micro/Nano machines driven by ultrasound power sources," *Chemistry - An Asian Journal* **14**, 2406–2416 (2019).
 - ⁴⁴ S. Tang *et al.*, "Structure-dependent optical modulation of propulsion and collective behavior of acoustic/light-driven hybrid microbowls," *Advanced Functional Materials* **29**, 1809003 (2019).
 - ⁴⁵ F. Nadal and E. Lauga, "Asymmetric steady streaming as a mechanism for acoustic propulsion of rigid bodies," *Physics of Fluids* **26**, 082001 (2014).
 - ⁴⁶ J. F. Collis, D. Chakraborty, and J. E. Sader, "Autonomous propulsion of nanorods trapped in an acoustic field," *Journal of Fluid Mechanics* **825**, 29–48 (2017).
 - ⁴⁷ C. Zhou, L. Zhao, M. Wei, and W. Wang, "Twists and turns of orbiting and spinning metallic microparticles powered by megahertz ultrasound," *ACS Nano* **11**, 12668–12676 (2017).
 - ⁴⁸ D. Ahmed, M. Lu, A. Nourhani, P. E. Lammert, Z. Stratton, H. S. Muddana, V. H. Crespi, and T. J. Huang, "Selectively manipulable acoustic-powered microswimmers," *Scientific Reports* **5**, 9744 (2015).
 - ⁴⁹ L. Ren, N. Nama, J. M. McNeill, F. Soto, Z. Yan, W. Liu, W. Wang, J. Wang, and T. E. Mallouk, "3D steerable, acoustically powered microswimmers for single-particle manipulation," *Science Advances* **5**, eaax3084 (2019).
 - ⁵⁰ J. Li, T. Li, T. Xu, M. Kiristi, W. Liu, Z. Wu, and J. Wang, "Magneto-acoustic hybrid nanomotor," *Nano Letters* **15**, 4814–4821 (2015).
 - ⁵¹ L. Ren, W. Wang, and T. E. Mallouk, "Two forces are better than one: combining chemical and acoustic propulsion for enhanced micromotor functionality," *Accounts of Chemical Research* **51**, 1948–1956 (2018).
 - ⁵² K. J. Rao, F. Li, L. Meng, H. Zheng, F. Cai, and W. Wang, "A force to be reckoned with: a review of synthetic microswimmers powered by ultrasound," *Small* **11**, 2836–2846 (2015).
 - ⁵³ K. Kim, J. Guo, Z. Liang, F. Zhu, and D. Fan, "Man-made rotary nanomotors: a review of recent developments," *Nanoscale* **8**, 10471–10490 (2016).
 - ⁵⁴ X.-Z. Chen, B. Jang, D. Ahmed, C. Hu, C. De Marco, M. Hoop, F. Mushtaq, B. J. Nelson, and S. Pané, "Small-scale machines driven by external power sources," *Advanced Materials* **30**, 1705061 (2018).
 - ⁵⁵ H. Bruus, "Acoustofluidics 7: The acoustic radiation force on small particles," *Lab on a Chip* **12**, 1014–1021 (2012).
 - ⁵⁶ S. B. Barnett, G. R. Ter Haar, M. C. Ziskin, H. D. Rott, F. A. Duck, and K. Maeda, "International recommendations and guidelines for the safe use of diagnostic ultrasound in medicine," *Ultrasound in Medicine & Biology* **26**, 355–366 (2000).
 - ⁵⁷ L. D. Landau and E. M. Lifshitz, *Fluid Mechanics*, 2nd ed., Landau and Lifshitz: Course of Theoretical Physics, Vol. 6 (Butterworth-Heinemann, Oxford, 1987).
 - ⁵⁸ H. G. Weller, G. Tabor, H. Jasak, and C. Fureby, "A tensorial approach to computational continuum mechanics using object-oriented techniques," *Computers in Physics* **12**, 620–631 (1998).
 - ⁵⁹ J. Happel and H. Brenner, *Low Reynolds Number Hydrodynamics: With Special Applications to Particulate Media*, 2nd ed., Mechanics of Fluids and Transport Processes, Vol. 1 (Kluwer Academic Publishers, Dordrecht, 1991).
 - ⁶⁰ J. Voß and R. Wittkowski, "Hydrodynamic resistance matrices of colloidal particles with various shapes," preprint, arXiv:1811.01269 (2018).
 - ⁶¹ J. Voß, R. Jegggle, and R. Wittkowski, "HydResMat – FEM-based code for calculating the hydrodynamic resistance matrix of an arbitrarily-shaped colloidal particle," Zenodo (2019), DOI: 10.5281/zenodo.3541588.
 - ⁶² M. J. Holmes, N. G. Parker, and M. J. W. Povey, "Temperature dependence of bulk viscosity in water using acoustic spectroscopy," *Journal of Physics: Conference Series* **269**, 012011 (2011).
 - ⁶³ Y. Xie, N. Nama, P. Li, Z. Mao, P.-H. Huang, C. Zhao, F. Costanzo, and T. Huang, "Probing cell deformability via acoustically actuated bubbles," *Small* **12**, 902–910 (2015).
 - ⁶⁴ E. Lauga and T. R. Powers, "The hydrodynamics of swimming microorganisms," *Reports on Progress in Physics* **9**, 096601 (2009).
 - ⁶⁵ Z. Shen, A. Würger, and J. S. Lintuvuori, "Hydrodynamic interaction of a self-propelling particle with a wall," *European Physical Journal E* **41**, 39 (2018).
 - ⁶⁶ T. Nitschke and R. Wittkowski, "Collective guiding of acoustically propelled nano- and microparticles for medical applications," in preparation (2020).
 - ⁶⁷ H. Ceylan, I. C. Yasa, U. Kilic, W. Hu, and M. Sitti, "Translational prospects of untethered medical micro-robots," *Progress in Biomedical Engineering* **1**, 012002 (2019).
 - ⁶⁸ R. Wittkowski and H. Löwen, "Dynamical density functional theory for colloidal particles with arbitrary shape," *Molecular Physics* **109**, 2935–2943 (2011).
 - ⁶⁹ A. Tiribocchi, R. Wittkowski, D. Marenduzzo, and M. E. Cates, "Active Model H: scalar active matter in a momentum-conserving fluid," *Physical Review Letters* **115**, 188302 (2015).
 - ⁷⁰ J. Stenhammar, R. Wittkowski, D. Marenduzzo, and M. E. Cates, "Light-induced self-assembly of active rectification devices," *Science Advances* **2**, e1501850 (2016).
 - ⁷¹ R. Wittkowski, J. Stenhammar, and M. E. Cates, "Nonequilibrium dynamics of mixtures of active and passive colloidal particles," *New Journal of Physics* **19**, 105003 (2017).
 - ⁷² J. Bickmann and R. Wittkowski, "Predictive local field theory for interacting active Brownian spheres in two spatial dimensions," *Journal of Physics: Condensed Matter* **accepted** (2019), DOI: 10.1088/1361-648X/ab5e0e.
 - ⁷³ D. Saintillan, "Rheology of active fluids," *Annual Review of Fluid Mechanics* **50**, 563–592 (2018).
 - ⁷⁴ H. M. López, J. Gachelin, C. Douarche, H. Auradou, and E. Clément, "Turning bacteria suspensions into superfluids," *Physical Review Letters* **115**, 028301 (2015).